Microfluidics and Nanofluidics (2021) 25:57
https://doi.org/10.1007/s10404-021-02459-2

RESEARCH PAPER

Sorting of circulating tumor cells based on the microfluidic device of a biomimetic splenic interendothelial slit array

Jianfeng Chen[1,2] · Zefan Yang[1] · Wenhu Xu[1,2] · Meirong Yi[1,2] · Min Zhong[1,2] · Xiaobing Li[1,2] · Hongwei Tian[3]

Received: 5 February 2021 / Accepted: 7 June 2021 / Published online: 12 June 2021

Abstract

In this paper, we focused on a microfluidic sorting method based on bionic splenic sinus microstructures to capture circulating tumor cells (CTCs). A dynamic multiphase fluidic model was developed to explore the effects of different flows and the parameters of the spleen-specific structure of the interendothelial slit (IES) on the cell membrane strain, as represented by the interface area between two phases. The results indicated that parameters of the IES and flow velocity strongly influence cell membrane strain. The biomimetic IES structure has more advantages than do circular pores because the slit structure has a lower flow resistance compared to the circle structure. A microfluidic device based on a biomimetic IES with ultrathin (500 nm thick) silicon nitride filters was designed and fabricated for high-throughput enrichment of high-viability CTCs. The silicon nitride filters had areas as large as 36 mm^2 (6 × 6 mm) and included nearly 18,000 slit units, which was conducive to obtaining a high-throughput device. Moreover, the effects of different parameters, such as velocity, slit width, dilution ratio and solution volume, on the cell capture efficiency and cell viability were explored. The results show that the microfluidic device based on a biomimetic IES has a high potential for preserving viable cells. This study quantitatively explored the effects of different parameters on cell viability during the CTC physical filtration process. Additionally, this study will be helpful for designing high-throughput CTC enrichment devices that capture high-viability cells.

Keywords CTCs · Splenic interendothelial slit · Viability · High throughput · Sorting

1 Introduction

Cancer is a high-mortality disease that has attracted increasing attention. A great danger of cancer is that cancer cells can spread from the original organ to other organs through blood or lymphatic system in a process called cancer metastasis (Kitamura et al. 2015). Cancer cells that detach from primary tumors and circulate in peripheral blood are called circulating tumor cells (CTCs) (Williams 2013; Plaks and Werb 2013), which include much information about the genes and pathology of patients and are helpful in diagnosis and therapy (Smirnov et al. 2005). These findings suggest that CTCs can be used as cancer biomarkers in medical diagnoses (Cristofanilli et al. 2005), cancer mechanism studies (Cristofanilli et al. 2004) and other areas. However, CTCs are extremely rare, with only hundreds of CTCs per milliliter of blood (Alix-Panabières and Pantel 2013). A process to enrich CTCs from whole blood has to be performed before other CTC pathological analyses. In addition, the difficulties in separating viable CTCs restrict further analysis, such as gene and drug experiments (Paterlini-Brechot and Benali 2007). As techniques have become more advanced, CTC enrichment methods have been developed quickly (Alix-Panabieres and Pantel 2014). Thus far, the CTC enrichment methods can be grouped into two categories: biochemical methods and physical methods (Alix-Panabieres and Pantel 2014). Biochemical methods capture target cells by specific antibody–antigen interactions, including epithelial cell adhesion molecules (EpCAM) and other biochemical molecules (Königsberg et al. 2011; Stott et al. 2010; Li et al. 2015; Lv et al. 2015). To date, the only FDA-approved CTC separation system is the CellSearch® system (Raritan, NJ, USA), which is a representative biochemical method (Riethdorf

✉ Wenhu Xu
flipreverse@126.com

1 Department of Mechanical Engineering, Nanchang University, Nanchang, Jiangxi Province, China

2 Key Laboratory of Tribology, Nanchang University, Nanchang, Jiangxi Province, China

3 School of Materials Science and Engineering, Jilin University, Changchun, Jilin Province, China

et al. 2007). The CellSearch® system captures target cells that express EpCAM molecules by using immunomagnetic beads. However, during the metastatic process, tumor cells will undergo epithelial-to-mesenchymal transition (EMT) and no longer express significant markers, such as EpCAM (Rao et al. 2005; Zheng et al. 2015; Gorges et al. 2012). Unfortunately, this EMT problem is a fundamental limitation of biochemical methods and cannot be avoided. Moreover, maintaining the viability of CTCs captured by immunomagnetic beads is difficult due to irreversible antibody–antigen binding.

Many enrichment methods based on the differences in physical properties between CTCs and normal blood cells, such as cell density (Park et al. 2012), size and deformability (McFaul et al. 2012; Kim et al. 2014; Li et al. 2014; Hvichia et al. 2016; Meunier et al. 2016) and dielectric properties (Warkiani et al. 2016, 2014; Okano et al. 2015), have been developed and have achieved considerable gains (Patil et al. 2015). These physical enrichment methods have two significant advantages over biochemical methods. The first advantage is that most physical separation methods do not require labels, which is extremely important for subsequent analyses that require viable and unperturbed cells. The second advantage is that physical methods require less time than biochemical methods because cancer cells do not need to be marked. Benefiting from high-throughput and mature techniques, the microfiltration method is a widely used method among physical enrichment methods (Zhou et al. 2014; Lin et al. 2010; Zheng et al. 2011). Microfilters with different materials and different structure parameters were developed to capture CTCs and have achieved gratifying successes. A commercially available type of filter, the polycarbonate track etch filter was fabricated for CTC capture. However, the track etch filter has two great disadvantages: low porosity (3–5%) and nonuniform, randomly distributed pores that limit the throughput and capture performance of enrichment devices (Fleischer et al. 1972). To overcome the abovementioned disadvantages, photolithographic fabrication was introduced to produce uniformly patterned microfilters from different materials, such as parylene (Zhou et al. 2014), PEGDA (Tang et al. 2014), SU-8 (Kang et al. 2015), PDMS (Fan et al. 2015), silicon (Lim et al. 2012), silicon nitride (Coumans et al. 2013; Kuiper et al. 1998; Van Rijn et al. 1997; Van Rijn and Elwenspoek 1995) and nickel (Hosokawa et al. 2010), for CTC enrichment. However, most studies of microfilters focus on improving the capture rate, purity and throughput of CTC enrichment devices. At present, the size-based method which has the characteristics of low cost and portability is widely used in CTCs sorting. However, although the average diameter of circulating tumor cells is larger than that of white blood cells, there is still the problem of overlapping diameters, which leads to a low efficiency of sorting circulating tumor cells. In addition, the researchers combined the difference in deformability between circulating tumor cells and leukocytes to further develop a sorting method based on size and deformability. However, this method may still have the problem of losing CTCs. Although cell viability is extremely important for subsequent analyses, few studies of microfilters have focused on improving cell viability. The major factor that affects cell viability in the physical enrichment process is the cell membrane rupture of CTCs. Zheng and his coworkers fabricated 3D microfilters (Zhou et al. 2014; Zheng et al. 2011) and flexible microspring array devices (Harouaka et al. 2014) to reduce the cell membrane deformability and capture viable CTCs. However, the authors considered only the influence of static pressure on CTC viability. In addition, the parameter structure of the filter still needs to be optimized.

Compared to a static simulation of the pressure of a flow field, a dynamic model can offer more information and a better analysis. Because the interaction between cells and microfluidic devices is considered at the cellular level, the influence of internal cellular structures, such as the cytoskeleton, can be ignored. Generally, cells are modeled as continuous materials that can be grouped into two categories: a solid model and a liquid model. Compared to the solid model, the liquid model has the advantage of large deformation. Zhang et al. developed a liquid model to explore the effects of a 3D confinement geometry on the pressure on CTCs passing through a channel (Zhang et al. 2014; Aghaamoo et al. 2015). However, the dynamic membrane strain of cells during the separation process, which can directly affect cell viability, was not explored.

The spleen, which is about 10–12 cm long and weighs 200 g is located in the upper left abdomen. It is the largest immune organ in the human body and plays an important role in the immune system. Meanwhile, the spleen is also a filter that can remove aging and diseased red blood cells from the circulatory system (Pivkin et al. 2016). When the shape, size or deformability of red blood cells changes, the spleen will prevent these red bloods cells from passing through (Li et al. 2018). The physical filtering function of the spleen is determined by the microscopic interstitial structure of the splenic sinus, which is the narrowest circulatory bottleneck in the vascular system (Duez et al. 2018). The splenic sinus is characterized by a high-aspect ratio interendothelial slit (IES), with only a submicron thickness (0.2–0.8 microns) and a micron-sized length and height (3–5 microns).

Inspired by the function of the splenic sinus in filtering red blood cells, we studied a bionic splenic sinus microfluidic chip for capturing circulating tumor cells. We developed a dynamic multiphase fluidic model to explore the effects of different flows and the parameters of the spleen-specific structure of the interendothelial slit (IES) on the cell membrane strain. The simulation showed that compared to the

circular-pore structure, the interendothelial slit (IES) structure has advantages in terms of the porosity, throughput and cell viability. Moreover, we designed and fabricated a bionic splenic sinus microfluidic device for CTC separation with slit filters prepared from ultrathin silicon nitride due to the excellent properties of silicon nitride, such as its high structural strength, transparency and good biocompatibility. This device showed strong performance with high enrichment efficiency, high throughput and high cell viability. This work has the potential to solve the critical problem of CTC viability after separation.

2 Materials and methods

2.1 Definition of cell membrane rupture

During a physical separation process, cells will experience pressure from the fluid and from the interaction force between cells and filters, which will cause cell membrane deformation. The total dynamic CTC separation process can be divided into two processes. The first process starts when the cells begin to interact with the filter and continues until the cells are fully captured; cells experience dynamic pressure during this first process. The second process starts when the cells are fully captured and continues until the end of the whole separation process; cells experience static pressure during this second process (Zheng et al. 2011). The cell membrane deformation is larger in the second process than in the first process. Previously, micropipette experiments showed that cells will rupture when the deformation of the cell membrane is over 6% (Hategan et al. 2003; Evans and Ludwig 2000; Waugh 2014). Consequently, we consider 6% cell membrane strain as the critical strain value; higher values can be regarded as indicating cell rupture in the simulation.

2.2 Simulation description and settings

A volume of fluid (VOF) model was applied to explore the deformation of cells traversing the IES filters or the circular-pore filters (Fig. 1). The VOF model tracks the insoluble interface formed by two phases, which can be described as the cell membrane. The volume fraction of the primary phase (α) varies between 0 and 1. A two-equation turbulence model named the realizable k-ε model is used for numerical accuracy; in this model, the turbulence kinetic energy, k, and its rate of dissipation, ε, are introduced. In addition, the Pressure-Implicit with Splitting of Operators (PISO) scheme that is suitable for transient computation is employed for pressure–velocity coupling. Additionally, the Pressure Staggering Options (PRESTO) method was applied for the pressure, and the Geo-Reconstruct method was applied for volume fraction spatial discretization. Both methods are available in Fluent. For the boundary settings, the inlet of the channel is set to have a constant flow rate, and the outlet is set as a pressure outlet. The periodic boundary condition is applied at the lateral face of the fluid body, while no-slip and stationary conditions are applied at the channel walls. Because of the periodic boundary condition at the lateral fluid boundary, the filtering film is considered infinite in our simulation.

In accordance with the properties of human blood, the fluid density is set as 1025 kg/m^3 and the dynamic viscosity is 3×10^{-3} Pa•s. The contact angle between a cell and the filter in the model is 180°, which means that cells do not adhere to the filter wall. The typical value of the surface tension of white blood cells (WBCs), 30×10^{-6} N/m, from previous literature is used in our model for convenience (Van

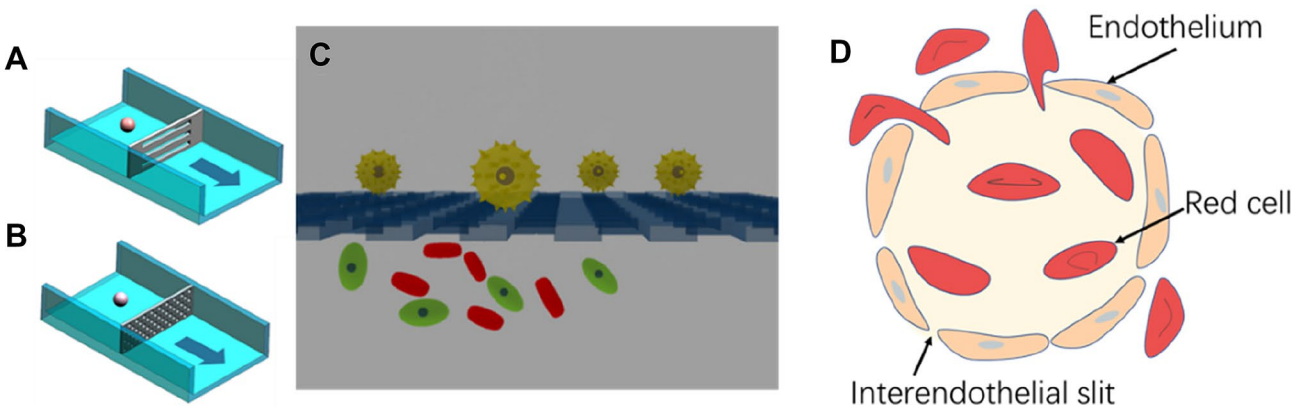

Fig. 1 Schematic diagram of the microfluidic device of bionic spleen IES for CTCs sorting. (**A**) Simulation model of the IES structure. (**B**) Simulation model of circular pores. (**C**) Schematic of the CTCs physical filtration method using the bionic IES microfluidic device. (**D**) Schematic of the structure of the spleen sinus

Rijn and Elwenspoek 1995; Hosokawa et al. 2010). Due to the wide variations in individual samples, the CTCs mechanical properties reported by different studies vary greatly from close to the value for WBCs to a value corresponding to a nearly 10 times higher stiffness than that of WBCs (McFaul et al. 2012; Shaw et al. 2015).

We simulated the influences of different IES parameters, such as the filter geometry, filter thickness and cell surface tension, on the cell membrane strain. Here, we compared two filter geometries: IES and circular pores. For a meaningful comparison of microfiltering films composed of an array of circular and IES pores, we fixed the porosity and characteristic dimensions of the microfilters at constant values. The diameter of the circular pore and the width of the slit pore were set to 7 μm.

2.3 Design and fabrication of the bionic splenic sinus microfluidic device for CTCs separation

The bionic splenic sinus microfluidic device is designed with a sandwich structure that consists of three parts: the top layer and the bottom layer are PDMS chambers, and the filtration membrane is located between these layers. The PDMS chambers contains a microfluidic channel connected to the filtration membrane, the top chamber is the CTC capture chamber, and the bottom chamber is the waste chamber.

The top and bottom chambers were fabricated with standard soft lithography. A 10 mm × 10 mm square silicon chip and a 400 μm thick SU-8 pattern was used as a mold. A PDMS prepolymer mixture (curing agent to PDMS ratio of 1:10, Sylgard 184, Dow Corning) was poured onto the mold and degassed in a vacuum chamber for 30 min. After curing on a 70 °C hotplate for 2 h, the PDMS was peeled from the mold and prepared for the next step. Then, the fabricated PDMS chambers were cured by O_2 plasma and subsequently combined with the filtration membrane.

Inspired by the splenic sinus structure, we introduced the IES as the filtration unit. The width of the slit filter, which is the critical dimension, ranges from 5 to 8 μm, and slit filters with a length of 100 μm are designed. Because silicon nitride films are transparent, stable and nonfluorescent, a monolayer patterned silicon nitride structure was designed as the filtration membrane. Furthermore, silicon nitride films have high tensile strength, which allows high porosity with a large filtration area, obviating complicated mounting procedures or additional support structures. The membrane area was 6 mm × 6 mm, and the thickness was 500 nm. Large and stiff cells will be captured on top of the membrane. The filtration membrane was fabricated by the microfabrication process shown in Fig. 2. First, a silicon nitride film with a specific tensile stress was deposited on the silicon substrate (400 μm in thickness) by PECVD. The thickness of the silicon nitride film (500 nm) was controlled by the deposition time, and the magnitude of the stress was controlled by the deposition parameters. Second, a 2 μm thick silicon oxide layer was deposited by PECVD on the back side of the silicon substrate as an etching resistance layer. Then, the high-resolution positive photoresist AZ6112 was spin coated onto the silicon nitride film. The ultraviolet aligner (SUSS MA 6) was used to expose the photoresist layer, which was covered by a chrome mask with a specific array pattern. AZ-MIF 400 solution was used for the photoresist development, and deionized water was used for cleaning the wafer after development. Then, the wafer was baked using a hot plate at 120 °C for 2 min. Afterwards, the array pattern was transferred from the photoresist layer to the silicon nitride membrane by reaction ion etching (RIE, OXFORD). The back side of the silicon oxide layer was also patterned to form etching windows by lithography and RIE etching. The photoresist was 10 μm thick AR-P 3210 (positive photoresist) and developed in AR 300-26 solution. It should be noted that there is no need to post-bake for AR-P 3210 because high temperatures will deform the pattern of the photoresist. The patterned silicon oxide layer produced by RIE provides resistance together with AR-P 3210 for bulk silicon etching. Afterwards, inductive coupling plasma etching (ICP etching) was used to etch most of the bulk silicon (380 μm in thickness). The residual bulk silicon (20 μm) was etched by KOH solution.

2.4 Cell culture

MDA-MB-231 cells were chosen for enrichment tests. The cancer cells (Cell Bank of the Chinese Academy of Sciences, China) were cultured in DMEM supplemented with 1% streptomycin/penicillin and 10% fetal bovine serum (all from Gibco, USA) and incubated at 5% CO2 at 37 °C in 35 mm dishes (Thermo Fisher Scientific, USA). The cells were treated with Trypsin–EDTA (Gibco, USA) solution for 1 min to form cell suspensions and then centrifuged at 1000 revolutions per minute (rpm) for 5 min to be harvested. The cells were then immersed in fresh DMEM and aspirated by gentle pipetting to form cell suspensions again. Prior to each experiment, the cells were trypsinized and resuspended in PBS or healthy human peripheral blood. The cells were counted with the standard plate-counting method by hand, and counting was repeated at least three times to account for operational errors.

2.5 Spiking of cancer cells

Cell concentrations were first determined by manual counting using a hemocytometer, and the cells were serially diluted with Dulbecco's phosphate-buffered saline (DPBS; PAA Laboratories GmbH) to an approximate concentration of 100 cells per well. Subsequently, the actual number of

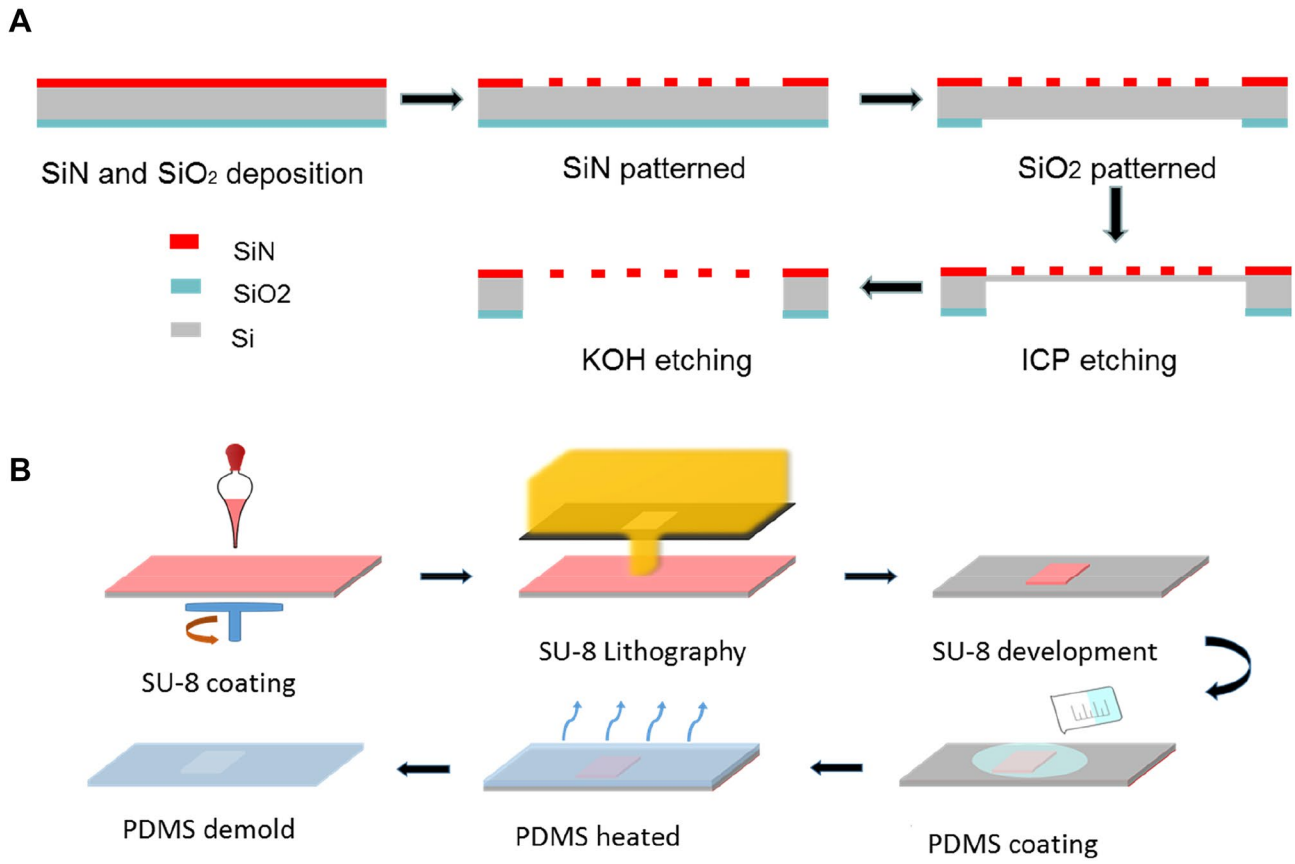

Fig. 2 Fabrication process of the bionic IES microfluidic device. (**A**) Fabrication process of the silicon nitride filtration membrane. (**B**) Fabrication process for the PDMS chamber

cells present in the suspension was determined by aliquoting cell suspensions (100 µL) into a 96-well plate and manually counting the cells under a microscope. The cell counting was repeated at least three times, and the count was averaged from 5 wells to minimize the effect of operational errors. A cell suspension volume corresponding to 100 cells was spiked into 1 mL of healthy human whole blood diluted with various volumes (0–2 mL) of PBS wash buffer (DPBS with 2 mM ethylene diamine tetra acetic acid (EDTA); Promega, USA) and 0.5% bovine serum albumin (BSA; Sigma-Aldrich, USA)).

2.6 Method for characterizing cell viability

Approximately, 100 MDA-MB-231 breast cancer cells were spiked into 1 mL of DPBS solution and passed through the filters. Then, 1 mL of pure DPBS solution was pumped into the filtration device to wash the channel and filters. After the abovementioned process, the LIVE/DEAD assay (Invitrogen, Carlsbad CA) was used for cell staining. The viable cells were stained by Calcein-AM green (8 µM) and showed green emission, and the dead cells were stained by ethidium homodimer-1 (EthD-1, 4 µM) and showed red emission in a fluorescence microscope.

2.7 Human blood samples

Healthy human whole blood samples (anticoagulated with EDTA) were provided by consenting donors at the Anhui Provincial Hospital by a standard protocol. Then, the whole blood samples were saved in a collection tube with EDTA to prevent coagulation. Subsequently, the blood samples were preserved in a − 4 °C refrigerator. All blood samples were used within 24 h for experiments. Portions of the blood samples were diluted multiple times with PBS wash buffer solution to determine the influence of blood concentration on the separation effect. The ratios of blood sample to PBS solution were 1:0, 1:1, 1:2, 1:5, and 1:10.

2.8 Flow characterization

The flow rate through the microfilters was controlled with a microinjection pump (SPLab02, Baoding Shenchen Precision Pump Co. Here, we set the flow rate to 0.1, 0.2,

0.5, 1 and 2 mL/min for the purpose of examining the influence of flow rate on separation efficiency.

2.9 Data processing and statistical analysis

Fiji/ImageJ (National Institutes of Health, USA) was used for image postprocessing. Origin (Origin Lab, USA) was used to perform statistical analysis and create graphs. All images were acquired with a Leica DMI3000B (Leica, Germany) microscope using the phase contrast and fluorescence modes. Cell counting and fluorescence in situ hybridization imaging were performed with 10x, 20x and 40x objective lenses.

3 Results and discussion

3.1 Theoretical calculations

The pore shape, size and distribution of filters strongly affect the separation results and fluidic performance. First, we analyzed the influence of different pore shapes on the pressure drop across the filters using the theoretical formula (Shown in Fig. 3). Both the width of the IES and the circular pore diameter are 7 μm. The flow rate (Q) is proportional to the pressure drop (Δp), as described by the following relationship (Kuiper et al. 2002):

$$\mathrm{Q} = \frac{\Delta p}{R}, \tag{1}$$

where R is the flow resistance.

3.2 Flow resistance

The flow resistance of a circular pore (R_c) can be calculated by the following formula (Kuiper et al. 2002):

$$R_c = \left\{ \frac{128h\eta}{\pi d^4} + \frac{24\eta}{d^3} \right\} f(\kappa_c), \tag{2}$$

where h and d are the thickness of the membrane and the diameter of the pore, respectively, and η is the viscosity of the liquid.κ_c is the porosity of circular pores on the membrane. $f(\kappa_c)$ is a factor that corrects for the synergetic effect of the pore array.

The flow resistance of a IES structure (R_s) can also be calculated by a similar formula (Kuiper et al. 2002):

$$R_s = \left\{ \frac{12h\eta}{ld^3} + \frac{32\eta}{\pi ld^2} \right\} g(\kappa_s), \tag{3}$$

where l and d are the length and width of the slit, respectively.κ_s is the porosity of slits on the membrane. $g(\kappa_s)$ is a factor that corrects for the synergetic effect of the slit array.

First, we investigated the influence of the IES thickness on the flow resistance. When $h \geq d$, the flow resistance of both circular pores and slits is approximately proportional to the thickness of the membrane. Furthermore, when $h \ll d$, the influence of thickness on flow resistance can be ignored. Generally, the thickness of the splenic sinus structure is on the submicron level, which means that the splenic sinus structure not only has a low flow resistance but also has a high flux. Hence, a membrane thickness of 500 nm will be optimal because both the flow resistance and strength of the membrane are considered.

Second, the flow resistance characteristics of the IES structure and the circular pore were compared. Here, both the factor f(κ_c) and g(κ_s) are set to 1, and the influence of

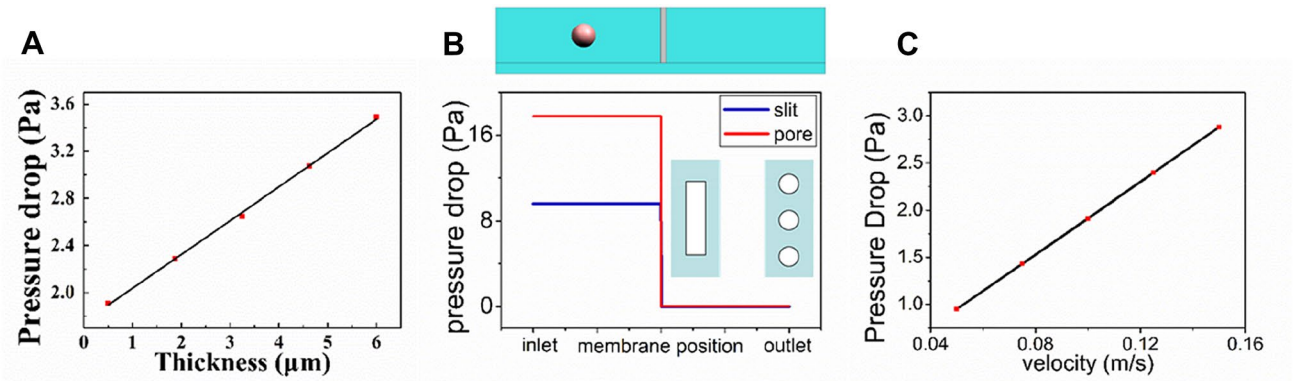

Fig. 3 Simulation of the effects of different parameters on the pressure drop across the filtration membrane. (**A**) Effect of filter thickness on the pressure drop across the membrane. (**B**) Effect of the filtration unit structure—IES or circular pore—on the pressure drop. (**C**) Effect of flow velocity on the pressure drop

thickness is ignored. Thus, expression (2) can be simplified as follows:

$$R_c = \frac{24\eta}{d^3}. \tag{4}$$

Expression (3) can be simplified as follows:

$$R_s = \frac{32\eta}{\pi l d^2}. \tag{5}$$

When we assume the same area for pores and slits and the same pressure drop, the ratio of Q_s to Q_c can be described as follows:

$$\frac{Q_s}{Q_c} = \frac{3\pi l}{4d} \times \frac{\pi\left(\frac{d}{2}\right)^2}{ld} = 1.85. \tag{6}$$

Hence, when the porosity and pressure drop are the same, the flow rate of the slit filter is 1.85 times that of circular pores.

3.3 VOF simulation results

A VOF multiphase model was developed to calculate the cell membrane strain during cell travel in the IES structure or the circular pore. To enrich the CTCs, WBCs (soft cells) should be separated and passed through the filter under the influence of a fluid force. Therefore, we performed a simulation and found the minimum flow rate that could push soft cells (WBCs) through the filter. The cell deformation at different times is shown in Fig. 4A, and the membrane strain during the process is shown in Fig. 4B. The maximum cell membrane strain occurred at the point when just half of the cell body passed through the filter. The maximum cell membrane strains under different flow rates with a 7 μm width slit and a 7 μm circular pore diameter are shown in Fig. 4C, D, respectively. The soft cell cannot pass through the 7 μm width IES when the velocity is less than 0.175 m/s. Correspondingly, a soft cell cannot pass through the 7 μm diameter pore when the velocity is less than 0.65 m/s. For both the slit filter and the pore filter, the cell membrane strain increases with increasing velocity. The thickness of the IES structure also influences the cell membrane strain under conditions with the same velocity (0.175 mm/s) (Fig. 4F, G). The maximum cell membrane strain increases when the IES thickness increases. Otherwise, as the slit width increased, the cell membrane strain decreased (Fig. 4H).

Notably, the minimum velocity (0.175 m/s) needed to force a soft cell to pass through the IES structure is less than the velocity (0.65 m/s) needed with a circular pore. Otherwise, the cell membrane strain (5.1%) is lower when passing through the IES filter than when passing through the circular pore (15.3%). This finding may be caused by the flow resistance being lower for a slit than for a circular pore. Additionally, the 15.3% cell membrane strain is considerably greater than the critical membrane rupture strain (6%). Thus, a lower velocity can be used to separate soft cells (WBCs) from stiff cells (CTCs) with the slit filter than with the circular-pore filter. This result means that compared with the circular-pore filter, the IES filter has a considerable advantage in

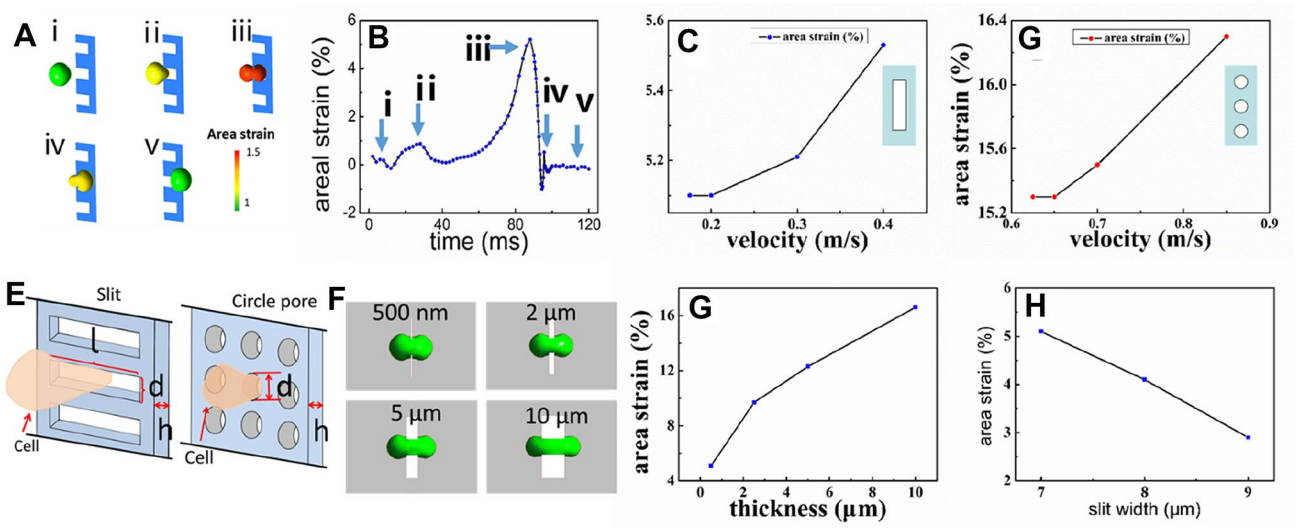

Fig. 4 Dynamic simulation of cells in the filtration process. (**A**) Simulated dynamic process of a cell passing through the IES filter. (**B**) The areal strain of cell during the dynamic process. (**C**) Effect of the flow velocity on the maximum cell membrane strain with an IES filter. (**D**) Effect of flow velocity on the maximum membrane strain with a circular-pore filter. (**E**) The schematic diagram of the filtering structural parameters. (**F**) Cell deformation under different thickness. (**G**) Effect of filter thickness on the maximum cell membrane strain. (**H**) Effect of slit width on the maximum cell membrane strain

preserving the cell activity. The IES filter thickness greatly influences the cell membrane strain, which varies from 5% for a 500 nm thickness to 16% for a 10 µm thickness. To keep the cell membrane strain under the critical strain (6%), the IES filter needs to be designed with a thickness of less than 1 µm.

3.4 The properties of the microfilter of the bionic IES

Silicon nitride is a suitable material for microscope imaging applications due to the optical features of transparent and nonfluorescent materials. Additionally, we can easily achieve a precise pattern and distribution on a silicon nitride membrane. Moreover, silicon nitride films deposited by plasma-enhanced chemical vapor deposition (PECVD) have high tensile stress, enabling high porosity in a large filtration area without the need for complex clamping devices and additional support structures. Bionic IES filters with widths ranging from 5 to 8 µm and a length of 100 µm were generated by an optical mask. Figure 5 shows an optical microscope image and scanning electronic microscope image of IES filters with a 6 µm width and ~ 18,000 slits in the 6 mm square membrane area. The slits are spaced at 20 µm intervals in the length direction and 10 µm intervals in the width direction. The porosity of the filters ranged from 23% (5 µm width) to 37% (8 µm width).

3.5 Separation performance of high-density IES filters

We studied the influence of size, flow rate, sample dilution and number of spiked cells on the efficiency of enrichment, which is defined as the ratio between the number of cells captured on filters and the number spiked in solution (Fig. 6). After enrichment, 1 mL of DPBS solution was used to wash the filters.

$$\text{Efficiency} = \frac{Number_{captured}}{Number_{spiked}} \times 100\%. \quad (7)$$

3.5.1 Effect of the IES width on the enrichment efficiency

The influence of slit width on the enrichment efficiency was explored using approximately 130 MDA-MB-231 cells spiked into 1 mL of DPBS (shown in Fig. 6A). IES filters with widths ranging from 5 to 8 µm were used to evaluate the enrichment efficiency, and the flow rate was 0.5 mL/min. Captured cells were observed and counted by using a fluorescence microscope. The experiments for measuring each parameter were repeated at least 3 times. The smaller was the IES width, the higher was the enrichment efficiency. The efficiency decreased from > 90% to < 70% as the slit width increased from 5 to 8 µm. However, a filter with a small slit width may intercept too many WBCs and cause low purity in

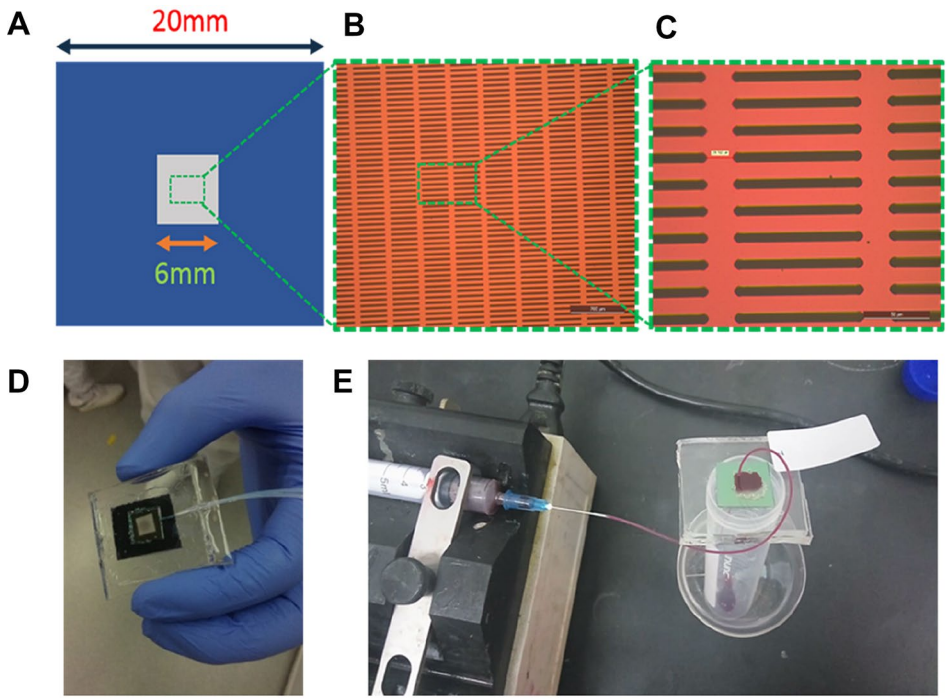

Fig. 5 Images of a silicon nitride membrane and the bionic splenic sinus microfluidic device. (**A**) Schematic of a silicon nitride membrane. (**B**) Image of a silicon nitride membrane with a slit array. (**C**) Magnified view of the indicated box in the slit array. (**D**) Image of the CTC enrichment device. (**E**) Image showing the CTC enrichment process

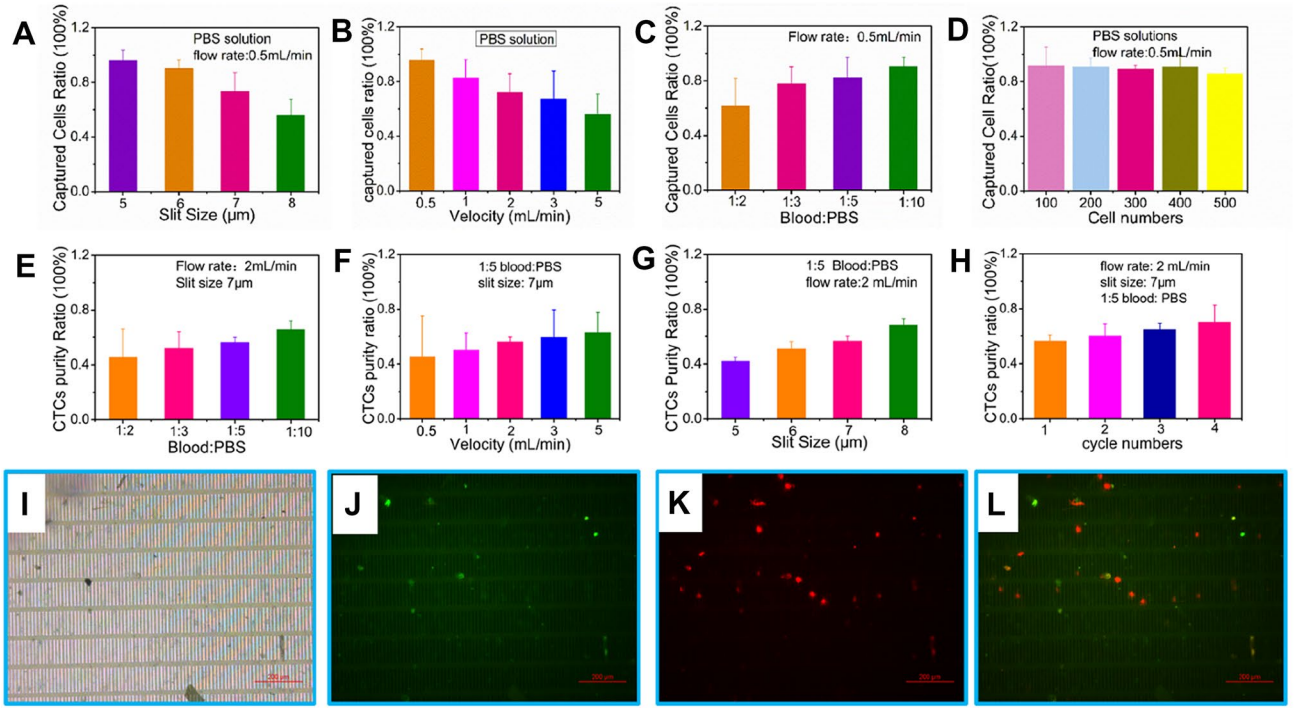

Fig. 6 Performance of the bionic splenic sinus microfluidic device based on the silicon nitride membrane. (**A**–**D**) Effect of different parameters on cell enrichment efficiency. (**A**) Effect of slit width on cell capture efficiency. (**B**) Effect of flow velocity on cell capture efficiency. (**C**) Effect of dilution ratio on cell capture efficiency. (**D**) Effect of cell number on cell capture efficiency. (**E**, **F**) Effect of different parameters on CTCs purity ratio. (**E**) Effect of dilution ratio on CTCs purity. (**F**) Effect of flow rate on CTCs purity ratio. (**G**) Effect of slit width on CTCs purity. (**H**) Effect of cycle numbers on CTCs purity. (**I**–**L**) Image of captured cancer cells and WBCs. (**I**) Bright field image. (**J**) Fluorescence image of captured WBCs. (**K**) Fluorescence image of captured cancer cells. (**L**) Merged bright field and fluorescence image

the CTC sample. Considering the balance among enrichment efficiency, purity and clogging, 7 μm is the optimal width.

3.5.2 Effect of flow rate on enrichment efficiency

The influence of flow rate on enrichment efficiency was also explored by using approximately 130 MDA-MB-231 cells spiked into 1 mL of DPBS (shown in Fig. 6B). Flow rates ranging from 0.5 to 5 mL/min were used to evaluate the enrichment efficiency with a slit width of 7 μm. As the flow rate increased, the enrichment efficiency decreased from ~ 90% to ~ 70%.

3.5.3 Effect of dilution ratio on enrichment efficiency

The effect of sample dilution ratio was also studied with 130 MDA-MB-231 cells spiked into a 1 mL blood sample diluted with different volumes of DPBS (1, 2, 3, 5 and 10 mL) (shown in Fig. 6C). The flow rate was 0.5 mL/min, and the slit width was 7 μm.

As the dilution volume of DPBS increased from 1 to 10 mL, the enrichment efficiency of cancer cells increased from ~ 70 to ~ 90%. This trend also confirms the findings of previous studies showing that diluting samples reduces the pressure drop and increases the enrichment efficiency.

Diluting samples reduces the viscosity of the fluid, which is proportional to the flow resistance. Hence, the pressure drop across the filter decreases when the dilution ratio increases. However, a high dilution ratio means that the total volume of the sample also increases, which will increase the processing time under conditions with the same flow rate.

3.5.4 Effect of cell number on enrichment efficiency

The number of CTCs varies greatly among different blood samples (shown in Fig. 6D). Here, we measured the enrichment efficiencies with different numbers of spiked cells (100, 200, 300, 400, 500 cells) in the same volume of DPBS solution. The flow rate was 0.5 mL/min, and the slit width was 7 μm. The efficiencies were almost unchanged for different numbers of cells.

The main reason is that the number of cells (mainly 10^2) is much less than the number of slits (10^5). Therefore, there is no significant change in the pressure drop across the filter when the enriched cells clog the slits.

3.5.5 Effect of the diluted ratio on the CTCs purity

The effect of diluted ratio on CTCs purity was also studied by spiked MDA-MB-231 cells (shown in Fig. 6E) in 1 mL diluted blood solution which's dilution ratios are 1:2,1:3,1:5,1:10, respectively. The flow velocity was set as 2 mL/min and the slit width was 7 μm. The percentage of spiked MDA-MB-231 cells among total cells (contained white blood cells) increased from 45 to 65% with the dilution ratios increased. This is because the greater the dilution ratio, the lower the number of white blood cells in the solution, so the higher the purity of CTCs.

3.5.6 Effect of the flow rate on the CTCs purity

The influence of flow rate on CTCs purity was also explored using approximately 130 MDA-MB-231 cells spiked into 1 mL of diluted blood solution (shown in Fig. 6F). Flow rates ranging from 0.5 mL/min to 5 mL/min were used to evaluate the CTCs purity with a slit width of 7 μm. As the flow rate increased, the CTCs purity increased from ~ 45.6 to ~ 63.4%. This is because white blood cells have a greater deformation force than CTCs, so at a high flow rate, more white blood cells are filtered out.

3.5.7 Effect of slit width on the CTCs purity

The influence of slit width on the CTCs purity was explored by using approximately 130 MDA-MB-231 cells spiked into 1 mL of diluted blood solution (shown in Fig. 6G). IES filters with widths ranging from 5 to 8 μm were used to evaluate the CTCs purity, and the flow rate was 2 mL/min. The experiments for measuring each parameter were repeated at least 3 times. The smaller was the IES width, the higher was the enrichment efficiency. The CTCs purity increased from 42 to 68% as the slit width increased from 5 to 8 μm. The filter with a small slit width may intercept too many WBCs and cause low purity in the CTC sample.

3.5.8 Effect of cycle numbers on the CTCs purity

Moreover, we explored the influence of cycle numbers on CTCs purity (shown in Fig. 6H). After cell filtration, rinse with PBS solution, and use 1 mL of PBS solution per cycle. The flow velocity was maintained at 2 mL/min. As the cycle number increased, the percentage of CTCs increased.

3.6 Characterization of cell viability

The membrane strain of cells is caused by the pressure drop across the filters, which is described as the flow rate divided by the flow resistance (Fig. 7). Therefore, the viability of cells increases as the pressure drop decreases.

3.7 Effect of the IES slit width on the cell viability

The effect of slit size on cell viability was studied by spiked MDA-MB-231 cells (Fig. 7A) in 1 mL of PBS solution. The flow velocity was set as 0.5 mL/min. With the slit width increased from 5 to 8 μm, the percentage of viable cells among total cells increased from 66 to 91%. This result agrees with the simulation showing that the pressure drop and cell membrane strain decrease with increasing slit width.

3.8 Effect of velocity on cell viability

The influence of flow velocity on cell viability was also explored by MDA-MB-231 cells (Fig. 7B) spiked in 1 mL of PBS solution. Here, the slit width was set to 7 μm. With increasing velocity, the percentage of viable cells decreased. This result also agrees with the simulation showing that the pressure drop and cell membrane strain increase with increasing velocity.

3.9 Effect of cycle numbers on cell viability

Moreover, we explored the influence of cycle numbers on cell viability. After cell filtration, rinse with PBS solution, and use 1 mL of PBS solution per cycle. The flow velocity was maintained at 0.5 mL/min. As the cycle number increased, the percentage of viable cells decreased greatly. This finding means that the flow duration greatly affects cell viability even with a low flow rate. Increasing the filter area and filter number might optimize the balance between the flow rate and duration.

4 Conclusion

Overall, inspired by the filtering function of the spleen, we developed a bionic splenic sinus microfluidic device for sorting CTCs. The multiphase fluidic model showed that with increasing flow rates and filter thicknesses or decreasing silt widths, the cell membrane strain increases. The IES filter has more advantages compared to the circular-pore filter for decreasing the cell membrane strain under the same fluidic parameters because the flow resistance is lower in the slit unit than in the circular-pore filter. In accordance with the simulation results, silicon nitride filters with slit arrays were designed and fabricated for viable and highly efficient cell enrichment. With increasing slit width and velocity or decreasing dilution ratio, the captured cancer cell ratio decreases. Moreover, as the slit width decreases or the velocity and the solution volume increase, the rate of viable cells decreases greatly. Our studies quantitatively analyzed the

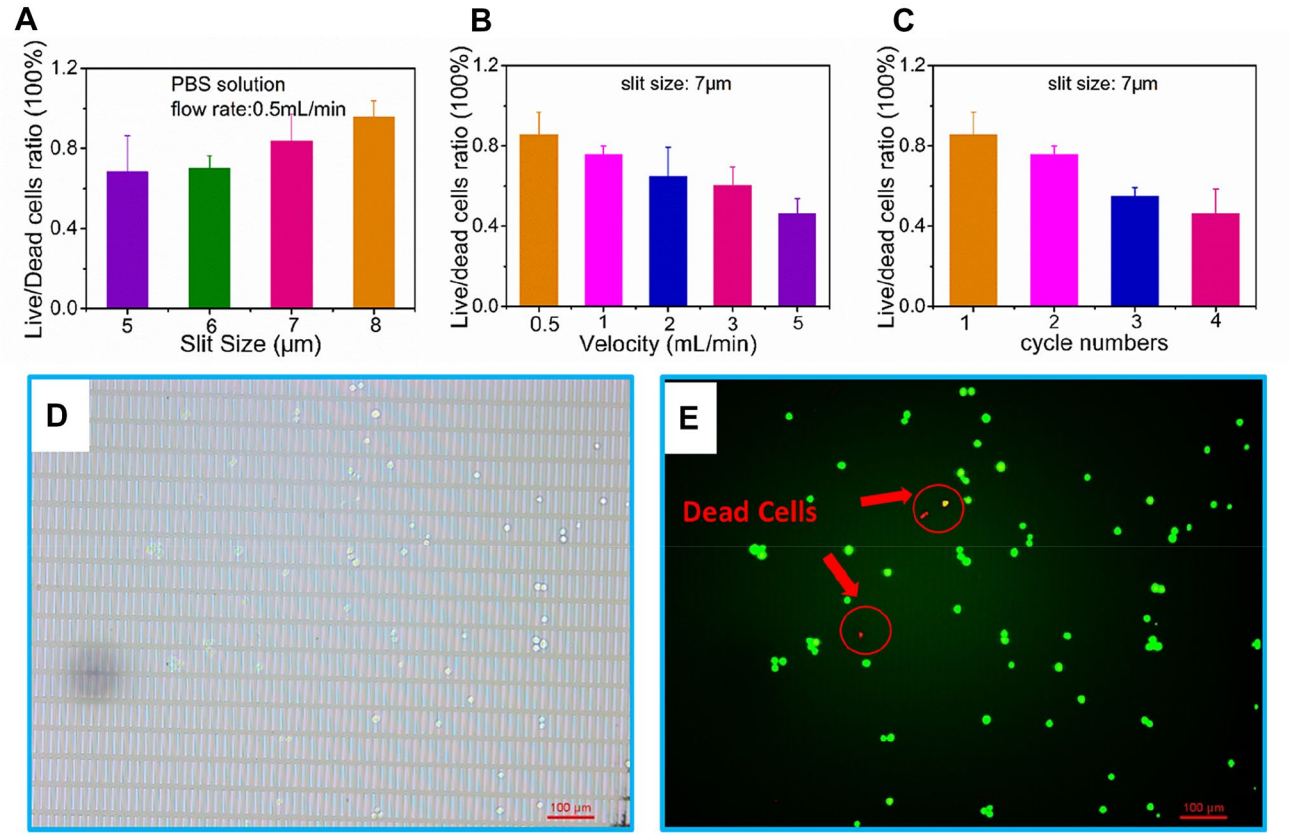

Fig. 7 Effect of the bionic splenic sinus microfluidic device on the cell viability. (**A**–**C**) Effects of different parameters on cell viability. (**A**) Effect of slit width on cell viability. (**B**) Effect of flow velocity on cell viability. (**C**) Effect of solution volume on cell viability. (**D**) Bright field image of captured cancer cells. (**E**) Merged image of the live cells and dead cells

effects of various parameters on cell viability. These bionic splenic sinus microfluidic devices have great potential for use in high efficiency techniques to enrich viable CTCs.

Acknowledgements This work is financially supported by the National Natural Science Foundation of China (No.51905248). This work was partially carried out at the USTC Center for Micro- and Nanoscale Research and Fabrication.

Declarations

Conflict of interest The authors declare no conflict of interest.

References

Aghaamoo M, Zhang ZF, Chen XL, Xu J (2015) Deformability-based circulating tumor cell separation with conical-shaped microfilters: Concept, optimization, and design criteria. Biomicrofluidics 9:034106

Alix-Panabières C, Pantel K (2013) Circulating tumor cells: liquid biopsy of cancer. Clin Chem 59:110–118

Alix-Panabieres C, Pantel K (2014) Challenges in circulating tumour cell research. Nat Rev Cancer 14:623–631

Coumans FA, Dalum GVD, Beck M, Terstappen LWMM (2013) Filter characteristics influencing circulating tumor cell enrichment from whole blood. PLoS ONE 8:61770

Cristofanilli M, Budd GT, Ellis MJ, Stopeck A, Matera J, Miller MC, Reuben JM, Doyle GV, Allard WJ, Terstappen LWMM, Hayes DF (2004) Circulating tumor cells: a novel prognostic factor for newly diagnosed metastatic breast cancer. N Engl J Med 351:781–791

Cristofanilli M, Hayes DF, Budd GT, Ellis MJ, Stopeck A, Reuben JM, Doyle GV, Matera J, Allard WJ, Miller MC, Fritsche HA, Hortobagyi GN, Terstappen LWMM (2005) Circulating tumor cells, disease progression, and survival in metastatic breast cancer. J Clin Oncol 23:1420–1430

Duez J, Carucci M, Garcia-Barbazan I, Corral M, Perez O, Presa JL, Henry B, Roussel C, Ndour PA, Rosa NB, Sanz L, Gamo FJ, Buffet P (2018) High-throughput microsphiltration to assess red blood cell deformability and screen for malaria transmission–blocking drugs. Nat Protoc 13:1362

Evans E, Ludwig F (2000) Dynamic strengths of molecular anchoring and material cohesion in fluid biomembranes. J Phys Condens Matter 12:A315

Fan XY, Jia CP, Yang J, Li G, Mao HG, Jin QH, Zhao JL (2015) A microfluidic chip integrated with a high-density PDMS-based microfiltration membrane for rapid isolation and detection of circulating tumor cells. Biosens Bioelectron 71:380–386

Fleischer RL, Alter HW, Furman SC, Price PB, Walker RM (1972) Particle track etching. Science 178:255–263

Gorges TM, Tinhofer I, Drosch M, Röse L, Zollner TM, Krahn T, Ahsen OV (2012) Circulating tumour cells escape from EpCAM-based detection due to epithelial-to-mesenchymal transition. BMC Cancer 12:178

Harouaka RA, Zhou MD, Yeh YT, Khan WJ, Das A, Liu X, Christ CC, Dicker DT, Baney TS, Kaifi JT, Belani CP, Truica CI, El-Deiry WS, Allerton JP, Zheng SY (2014) Flexible micro spring array device for high-throughput enrichment of viable circulating tumor cells. Clin Chem 60:323–333

Hategan A, Law R, Kahn S, Discher DE (2003) Adhesively-tensed cell membranes: lysis kinetics and atomic force microscopy probing. Biophys J 85:2746–2759

Hosokawa M, Hayata T, Fukuda Y, Arakaki A, Yoshino T, Tanaka T, Matsunaga T (2010) Size-selective microcavity array for rapid and efficient detection of circulating tumor cells. Anal Chem 82:6629–6635

Hvichia GE, Parveen Z, Wagner C, Janning M, Quidde J, Stein A, Müller V, Loges S, Neves RPL, Stoecklein NH, Wikman H, Riethdorf S, Pantel K, Gorges TM (2016) A novel microfluidic platform for size and deformability based separation and the subsequent molecular characterization of viable circulating tumor cells. Int J Cancer 138:2894–2904

Kang YT, Doh I, Cho YH (2015) Tapered-slit membrane filters for high-throughput viable circulating tumor cell isolation. Biomed Microdevices 17:7

Kim YJ, Koo GB, Lee JY, Moon HS, Kim DG, Lee DG, Lee JY, Oh JH, Park JM, Kim MS, Woo HG, Kim S, Kang P, Tae WC, Sim S, Park WY, Lee JG, Kim YS (2014) A microchip filter device incorporating slit arrays and 3-D flow for detection of circulating tumor cells using CAV1-EpCAM conjugated microbeads. Biomaterials 35:7501–7510

Kitamura T, Qian BZ, Pollard JW (2015) Immune cell promotion of metastasis. Nat Rev Immunol 15:73–86

Königsberg R, Obermayr E, Bises G, Pfeiler G, Dittrich C (2011) Detection of EpCAM positive and negative circulating tumor cells in metastatic breast cancer patients. Acta Oncol 50:700–710

Kuiper S, Van Rijn CJM, Nijdam W, Elwenspoek MC (1998) Development and applications of very high flux microfiltration membranes. J Membrane Sci 150:1–8

Kuiper S, Brink R, Nijdam W, Krijnen GJM, Elwenspoek MC (2002) Ceramic microsieves: influence of perforation shape and distribution on flow resistance and membrane strength. J Membrane Sci 196:149–157

Li X, Chen WQ, Liu GY, Lu W, Fu JP (2014) Continuous-flow microfluidic blood cell sorting for unprocessed whole blood using surface-micromachined microfiltration membranes. Lab Chip 14:2565–2575

Li W, Reátegui E, Park MH, Castleberry S, Deng JZ, Hsu B, Mayner S, Jensen AE, Sequist LV, Maheswaran S, Haber DA, Toner M, Stott SL, Hammond PT (2015) Biodegradable nano-films for capture and non-invasive release of circulating tumor cells. Biomaterials 65:93–102

Li H, Lu L, Li XJ, Buffet PA, Dao M, Karniadakis GE, Suresh S (2018) Mechanics of diseased red blood cells in human spleen and consequences for hereditary blood disorders. Proc Natl Acad Sci USA 115:9574–9579

Lim LS, Hu M, Huang MC, Cheong WC, Gan ATL, Looi XC, Leong SM, Koay ESC, Li MH (2012) Microsieve lab-chip device for rapid enumeration and fluorescence in situ hybridization of circulating tumor cells. Lab Chip 12:4388–4396

Lin HK, Zheng S, Williams AJ, Balic M, Groshen S, Scher HI, Fleisher M, Stadler W, Datar RH, Tai YC, Cote RJ (2010) Portable filter-based microdevice for detection and characterization of circulating tumor cells. Clin Cancer Res 16:5011–5018

Lv SW, Wang J, Xie M, Lu NN, Li Z, Yan XW, Cai SL, Zhang PA, Dong WG, Huang WH (2015) Photoresponsive immunomagnetic nanocarrier for capture and release of rare circulating tumor cells. Chem Sci 6:6432–6438

Mcfaul SM, Lin BK, Ma H (2012) Cell separation based on size and deformability using microfluidic funnel ratchets. Lab Chip 12:2369–2376

Meunier A, Castro JAH, Turner K, Li K, Veres T, Juncker D (2016) Combination of mechanical and molecular filtration for enhanced enrichment of circulating tumor cells. Anal Chem 88:8510–8517

Okano H, Konishi T, Suzuki T, Suzuki T, Ariyasu S, Aoki S, Abe R, Hayase M (2015) Enrichment of circulating tumor cells in tumor-bearing mouse blood by a deterministic lateral displacement microfluidic device. Biomed Microdevices 17:11

Park JM, Lee JY, Lee JG, Jeong H, Oh JM, Kim YJ, Park D, Kim MS, Lee HJ, Oh JH, Lee SS, Lee WY, Huh N (2012) Highly efficient assay of circulating tumor cells by selective sedimentation with a density gradient medium and microfiltration from whole blood. Anal Chem 84:7400–7407

Paterlini-Brechot P, Benali NL (2007) Circulating tumor cells (CTC) detection: clinical impact and future directions. Cancer Lett 253:180–204

Patil P, Kigga M, Kumeria T, Losic D (2015) Isolation of circulating tumour cells by physical means in a microfluidic device: a review. RSC Adv 5:89745–89762

Pivkin IV, Peng ZL, Karniadakis GE, Buffet PA, Dao M, Suresh S (2016) Biomechanics of red blood cells in human spleen and consequences for physiology and disease. Proc Natl Acad Sci USA 113:7804–7809

Plaks VKCD, Werb Z (2013) Circulating tumor cells. Science 341:1186–1188

Rao CG, Chianese D, Doyle GV, Miller MC, Terstappen LWMM (2005) Expression of epithelial cell adhesion molecule in carcinoma cells present in blood and primary and metastatic tumors. Int J Oncol 27:49–57

Riethdorf S, Fritsche H, Muller V, Rau T, Schindlbeck C, Rack B, Janni W, Coith C, Beck K, Janicke F, Jackson S, Gornet T, Cristofanilli M, Pantel K (2007) Detection of circulating tumor cells in peripheral blood of patients with metastatic breast cancer: a validation study of the Cell Search system. Clin Cancer Res 13:920–928

Shaw BJ, Byun S, Begum S, Miyamoto DT, Hecht VC, Maheswaran S, Stott SL, Toner M, Hynes RO, Manalis SR (2015) Ceramic microsieves: influence of perforation shape and distribution on flow resistance and membrane strength. Sci Rep 5:18542

Smirnov DA, Zweitzig DR, Foulk BW, Miller MC, Doyle GV, Pienta KJ, Meropol NJ, Weiner LM, Cohen SJ, Moreno JG, Connelly MC, Terstappen LWMM, O'Hara SM (2005) Global gene expression profiling of circulating tumor cells. Cancer Res 65:4993–4997

Stott SL, Hsu CH, Tsukrov DI, Yu M, Miyamoto DT, Waltman BA, Rothenberg SM, Shah AM, Smas ME, Korir GK, Floyd FP, Gilman AJ, Lord JB, Winokur D, Springer S, Irimia D, Nagrath S, Sequist LV, Lee RJ, Isselbacher KJ, Maheswaran S, Haber DA, Toner M (2010) Isolation of circulating tumor cells using a microvortex-generating herringbone-chip. Proc Natl Acad Sci USA 107:18392–18397

Tang YD, Shi J, Li SS, Wang L, Chen Y (2014) Microfluidic device with integrated microfilter of conical-shaped holes for high efficiency and high purity capture of circulating tumor cells. Sci Rep 4:6052

Van Rijn CJM, Elwenspoek MC (1995) Microfiltration membrane sieve with silicon micromachining for industrial and biomedical applications, IEEE 83

Van Rijn C, Van der Wekken M, Nijdam W, Elwenspoek M (1997) Deflection and maximum load of microfiltration membrane sieves made with silicon micromachining. J Microelectromech Syst 6:48–54

Warkiani ME, Khoo BL, Tan DSW, Bhagat AAS, Lim WT, Yap YS, Lee SC, Han JY, Lim CT (2014) An ultra-high-throughput spiral microfluidic biochip for the enrichment of circulating tumor cells. Analyst 139:3245–3255

Warkiani ME, Khoo BL, Wu LD, Tay AKP, Bhagat AAS, Han JY, Lim CT (2016) Ultra-fast, label-free isolation of circulating tumor cells from blood using spiral microfluidics. Nat Protocols 11:134–148

Waugh RE (2014) Forty-percent area strain in red cell membranes?-Doubtful. Biophys J 106:1834–1835

Williams SC (2013) Circulating tumor cells. Proc Natl Acad Sci USA 110:4861

Zhang ZF, Xu J, Hong B, Chen XL (2014) The effects of 3D channel geometry on CTC passing pressure - towards deformability-based cancer cell separation. Lab Chip 14:2576–2584

Zheng S, Lin HK, Lu B, Williams A, Datar R, Cote RJ, Tai YC (2011) 3D microfilter device for viable circulating tumor cell (CTC) enrichment from blood. Biomed Microdevices 13:203–213

Zheng X, Carstens JL, Kim J, Scheible M, Kaye J, Sugimoto H, Wu CC, LeBleu VS, Kalluri R (2015) Epithelial-to-mesenchymal transition is dispensable for metastasis but induces chemoresistance in pancreatic cancer. Nature 527:525–530

Zhou MD, Hao SJ, Williams AJ, Harouaka RA, Zheng SY (2014) Separable bilayer microfiltration device for viable label-free enrichment of circulating tumour cells. Sci Rep 4:10